

# PRIMA: Pre-training with Risk-integrated Image-Metadata Alignment for Medical Diagnosis via LLM

Yiqing Wang<sup>1</sup>, Chunming He<sup>1</sup>, Ming-Chen Lu<sup>2</sup>, Mercy Pawar<sup>2</sup>, Leslie Niziol<sup>2</sup>, Maria Woodward<sup>2</sup>, and Sina Farsiu<sup>1</sup>

<sup>1</sup> Duke University, Durham NC 27708, USA

{yq.wang, chunming.he, sina.farsiu}@duke.edu

<sup>2</sup> University of Michigan, Ann Arbor MI 48109, USA

{mingchlu, mpawar, lmniziol, mariawoo}@med.umich.edu

**Abstract.** Medical diagnosis requires the effective synthesis of visual manifestations and clinical metadata. However, existing methods often treat metadata as isolated tags, failing to exploit the rich semantic knowledge embedded in clinical descriptions. We propose PRIMA (Pre-training with Risk-integrated Image-Metadata Alignment), a framework that integrates domain-specific knowledge into multi-modal representation learning. We first curate an expert corpus of risk-disease correlations via Retrieval-Augmented Generation (RAG) to refine Clinical ModernBERT, embedding diagnostic priors into the text encoder. To bridge the modality gap, we introduce a dual-encoder pre-training strategy utilizing DINOv3 and our refined BERT, optimized by a suite of four complementary loss functions. These losses are designed to capture multi-granular semantic alignment and handle the ambiguity of clinical correlations through soft labels. Finally, we leverage Qwen-3 to fuse these aligned features for precise disease classification. Extensive experiments demonstrate that PRIMA effectively harmonizes pixel-level features with abstract clinical expertise, significantly outperforming other state-of-the-art methods. Notably, our framework achieves superior robustness without the need for massive data collection or exhaustive computational resources. Our code will be made public upon acceptance.

**Keywords:** Vision-Language Pre-training · Clinical Knowledge Integration · Medical Image Diagnosis.

## 1 Introduction

Medical imaging is central to clinical diagnosis, where experts synthesize information from multi-view scans and complementary metadata, such as patient risk factors. While deep learning has seen success, most methods remain limited to single-image analysis, overlooking the heterogeneous nature of real-world clinical data. This creates a significant gap between current algorithms and actual diagnostic protocols involving diverse imaging and structured risk profiles.

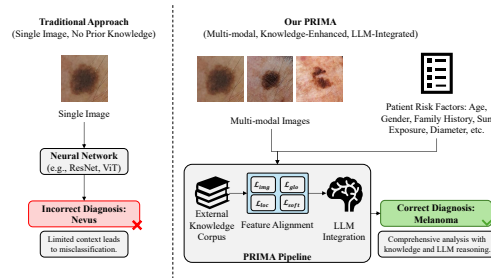


Fig. 1: Traditional vs. Our PRIMA Approach.

Furthermore, data scarcity remains a persistent barrier; despite recent efforts to curate large-scale medical datasets [21,10,19], relying on massive data is often infeasible for specialized tasks or rare diseases where patient cohorts are inherently limited.

Previous studies [13,17] have explored metadata fusion, yet these often rely on ad-hoc designs that impede generalizability across different clinical formats. Recent shifts toward Large Language Models (LLMs) and CLIP-based paradigms [18] offer robust representation capabilities but are typically data-intensive and sensitive to quality. Even with specialized medical adaptations [22,8,5], current methods remain heavily dependent on large-scale pre-training or fine-grained textual reports. Consequently, the rich semantic potential of structured clinical metadata remains largely underexplored, presenting a critical opportunity for more efficient, attribute-aware diagnostic frameworks.

In this paper, we propose PRIMA (Pre-training with Risk-integrated Image-Metadata Alignment), a framework designed to synergize domain-specific clinical knowledge with visual features (Fig. 1). To capture high-quality priors, we first construct a specialized knowledge bank of risk-disease relationships by leveraging GPT [15] and Gemini [3] via Retrieval-Augmented Generation (RAG) [1] on clinical literature. Subsequently, we fine-tune Clinical ModernBERT [7] on this corpus, circumventing the need for massive paired datasets by exploiting cost-effective expert literature to enhance semantic understanding. To bridge modality gaps, a dual-encoder pre-training stage utilizes DINOv3 [20] alongside our refined text encoder. We introduce four complementary objective functions to orchestrate the integration of diverse imaging modalities and textual knowledge at multiple scales. By harmonizing global context with fine-grained local features, this hierarchical alignment ensures robust adaptation to complex clinical scenarios. Finally, Qwen3 [24] aggregates these multi-modal features for precise disease diagnosis. Evaluations on PAD-UFES-20 [16] and AQUA show PRIMA significantly outperforms SOTA baselines without requiring massive data or exhaustive compute. Our contributions are summarized as follows:

- Knowledge-Enhanced Encoding: We elevate metadata to semantic knowledge by fine-tuning ClinicalBERT on RAG-derived corpora, explicitly injecting domain priors without requiring massive paired datasets.

- Multi-Granular Alignment: We propose a versatile strategy with four complementary losses to orchestrate global-local integration across diverse modalities, ensuring flexibility for heterogeneous clinical data.
- LLM-Driven Diagnosis: We introduce a unified pipeline leveraging Qwen3 to synthesize aligned features, achieving state-of-the-art performance and robust generalization on PAD-UFES-20 and AQUA datasets.

## 2 Method

Fig. 2 illustrates the overall architecture of PRIMA, which comprises three progressive training stages. First, we curate a domain-specific knowledge bank via Retrieval-Augmented Generation (RAG) using GPT [15] and Gemini [3] based on public literature. This corpus serves as the foundation for fine-tuning our text encoder, ClinicalBERT [7], to inject medical priors (Section 2.1). Next, we introduce a set of four complementary objective functions to orchestrate feature alignment across hierarchical semantic levels and diverse visual-textual perspectives (Section 2.2). Finally, a large language model is employed to synthesize the robust features extracted by the pre-trained encoders for precise diagnostic predictions (Section 2.3).

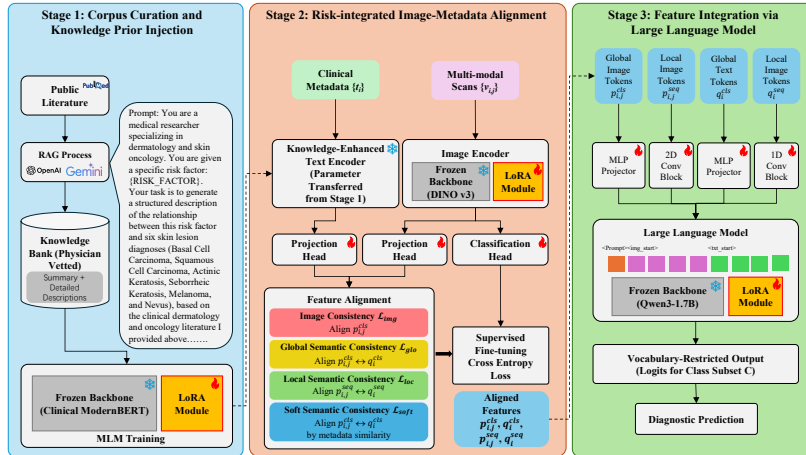


Fig. 2: Overview of our PRIMA.

### 2.1 Corpus Curation and Knowledge Prior Injection

While LLMs excel generally, they often falter in medical scenarios due to complex knowledge barriers. Clinical ModernBERT [7] partially mitigates this, yet it still struggles to capture fine-grained attribute correlations and rare pathologies.

Since data scarcity often hinders downstream fine-tuning, we leverage PubMed [11] literature to enhance semantic understanding. By retrieving task-specific articles (e.g., systematic reviews and case reports), we extract expert knowledge on risk-disease relationships, allowing our encoder to capture diagnostic priors without relying on scarce clinical data.

However, as clinical literature often presents correlations implicitly or contains conflicting evidence, we employ GPT-5.1 [15] and Gemini-2.5 [3] via Retrieval-Augmented Generation (RAG) [1] to synthesize these findings. RAG effectively mitigates hallucination by grounding model responses in the retrieved sources. As shown in Fig. 2, the LLMs generate structured descriptions—comprising a global summary and detailed paragraphs on specific risk factors—which are vetted by senior physicians to ensure accuracy. Following the Clinical ModernBERT protocol, we utilize Masked Language Modeling (MLM) [4] for knowledge injection. To maintain computational efficiency, we adopt LoRA [6], updating only 1% of the parameters while preserving pre-trained features.

## 2.2 Risk-integrated Image-Metadata Alignment

**Image and Text Encoder** We employ DINOv3 [20] and our knowledge-enhanced Clinical ModernBERT [7] as vision and text backbones. For the  $i$ -th patient, input data consists of multi-modal scans  $\{v_{i,j}\}_j$  and structured clinical metadata  $\{t_{i,k}\}_k$ . Guided by domain priors (Section 2.1), we filter for visually relevant attributes and concatenate them into a sequence  $t_i$ . The encoders extract latent features  $q_i \in \mathbb{R}^{(n+1) \times d}$  from text and  $p_{i,j} \in \mathbb{R}^{(m+1) \times d}$  from each image, where  $n, m$  denote sequence lengths and  $d$  is the latent dimension. Both modalities are mapped to a shared space via projection heads. At this stage, only the projection heads and LoRA [6] adapters in DINOv3 are trained (Fig. 2).

**Alignment Strategy** We decompose  $p_{i,j}$  and  $q_i$  into global class tokens ( $p_{i,j}^{cls}, q_i^{cls}$ ) and local sequence tokens ( $p_{i,j}^{seq}, q_i^{seq}$ ) to facilitate multi-granular alignment through four complementary objectives (Fig. 3). Image Consistency Loss ( $\mathcal{L}_{img}$ ) enforces intra-patient consistency by aligning global visual features across scans. Global Semantic Loss ( $\mathcal{L}_{glo}$ ) synchronizes visual and textual class tokens for high-level semantic alignment, while Local Semantic Loss ( $\mathcal{L}_{loc}$ ) captures fine-grained correlations between image patches and textual tokens. To handle clinical ambiguity, Soft Semantic Loss ( $\mathcal{L}_{soft}$ ) provides soft supervision via metadata-based similarity matrices. The final objective is a weighted sum of these losses. Following alignment, the image encoder undergoes supervised fine-tuning with ground-truth labels to sharpen its discriminative power.

- **Image Consistency Loss  $\mathcal{L}_{img}$ :** To enforce intra-patient visual consistency, we construct positive pairs by sampling either two distinct scans or a duplicated single scan from the same patient, applying independent random augmentations to each. The vision encoder extracts global class tokens from these views, and their similarity is measured via a temperature-scaled dot

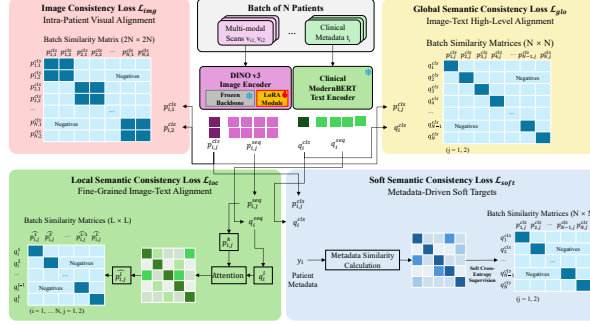


Fig. 3: Training Objectives of Our PRIMA.

product (Eq. 1) with hyperparameter  $\tau$ .

$$\text{sim}(x_1, x_2) = \frac{x_1^\top x_2}{\|x_1\| \|x_2\|} / \tau \quad (1)$$

For a batch of  $N$  patients, let  $p_{i,1}^{cls}$  and  $p_{i,2}^{cls}$  be global visual tokens from two views (distinct scans or augmentations) of patient  $i$ . Defined in Eq. 2,  $\mathcal{L}_{img}$  promotes patient-invariant representation learning by aligning latent features belonging to the same subject, where  $\mathcal{K}$  is the indication function.

$$\mathcal{L}_{img} = -\frac{1}{N} \sum_{i=1}^N \log \frac{e^{\text{sim}(p_{i,1}^{cls}, p_{i,2}^{cls})}}{\sum_{k=1}^N (e^{\text{sim}(p_{i,1}^{cls}, p_{k,2}^{cls})} + \mathcal{K}_{[k \neq i]} e^{\text{sim}(p_{i,1}^{cls}, p_{k,1}^{cls})})} \quad (2)$$

- **Global Semantic Loss  $\mathcal{L}_{glo}$ :** To establish a shared feature space, the Global Semantic Loss ( $\mathcal{L}_{glo}$ ) employs a symmetric cross-entropy objective (Eq. 3) over  $N$  matched global pairs  $\{(p_{i,j}^{cls}, q_i^{cls})\}_{i=1, j=1}^{N,2}$ . This synchronizes high-level semantic context, ensuring global visual embeddings capture the abstract clinical concepts encoded in the metadata.

$$\mathcal{L}_{glo} = -\frac{1}{4N} \sum_{i=1}^N \sum_{j=1}^2 \left( \log \frac{e^{\text{sim}(p_{i,j}^{cls}, q_i^{cls})}}{\sum_{k=1}^N e^{\text{sim}(p_{i,j}^{cls}, q_k^{cls})}} + \log \frac{e^{\text{sim}(q_i^{cls}, p_{i,j}^{cls})}}{\sum_{k=1}^N e^{\text{sim}(q_i^{cls}, p_{k,j}^{cls})}} \right) \quad (3)$$

- **Local Semantic Loss  $\mathcal{L}_{loc}$ :** To capture fine-grained correlations, we employ an attention-guided mechanism to synthesize a visual-word representation  $\hat{p}_{i,j}^l$  for each of the  $L$  text tokens  $q_i^{seq} = \{q_i^l\}_{l=1}^L$ . By using  $q_i^l$  as a query to attend to all  $K$  image patches  $p_{i,j}^{seq} = \{p_{i,j}^k\}_{k=1}^K$ , we aggregate the patches based on their relevance scores per Eq. 4.

$$\alpha_{l,k} = \frac{\exp(q_i^{l\top} p_{i,j}^k / \sqrt{d})}{\sum_{r=1}^K \exp(q_i^{l\top} p_{i,j}^r / \sqrt{d})}, \hat{p}_{i,j}^l = \sum_{k=1}^K \alpha_{l,k} p_{i,j}^k \quad (4)$$

Subsequently, we maximize the similarity between the original token  $q_i^l$  and its corresponding visual context  $\hat{p}_{i,j}^l$  while minimizing its similarity to other

tokens in the sequence, as formulated in Eq. 5. This mechanism effectively grounds abstract clinical attributes (e.g., irregular borders) onto their corresponding visual manifestations in the scan.

$$\mathcal{L}_{loc} = -\frac{1}{4LN} \sum_{l=1}^L \sum_{i=1}^N \sum_{j=1}^2 \left( \log \frac{e^{\text{sim}(q_i^l, \hat{p}_{i,j}^l)}}{\sum_{m=1}^L e^{\text{sim}(q_i^l, \hat{p}_{i,j}^m)}} + \log \frac{e^{\text{sim}(\hat{p}_{i,j}^l, q_i^l)}}{\sum_{m=1}^L e^{\text{sim}(\hat{p}_{i,j}^m, q_i^l)}} \right) \quad (5)$$

- **Soft Semantic Loss  $\mathcal{L}_{soft}$ :** To address the limitations of strict one-to-one mapping in standard contrastive losses, which neglect shared clinical attributes across patients, we introduce a soft-target alignment mechanism. We aggregate metadata into one-hot vectors  $y$ , upweighting disease-related dimensions (by a factor of 3) to prioritize diagnostic discriminability. A dynamic target distribution is then constructed via label sharpening:  $s_{i,j} = \text{Softmax}(\langle y_i, y_j \rangle / \tau_{label})$ , where  $\tau_{label}$  controls signal sparsity. Finally, the model minimizes the soft cross-entropy between this distribution and the predicted image-text similarities (Eq. 6).

$$\mathcal{L}_{soft} = -\frac{1}{4N^2} \sum_{i=1}^N \sum_{j=1}^N \sum_{k=1}^2 s_{i,j} \left( \log \frac{e^{\text{sim}(p_{i,k}^{cls}, q_j^{cls})}}{\sum_{t=1}^N e^{\text{sim}(p_{i,k}^{cls}, q_t^{cls})}} + \log \frac{e^{\text{sim}(q_j^{cls}, p_{i,k}^{cls})}}{\sum_{t=1}^N e^{\text{sim}(q_j^{cls}, p_{t,k}^{cls})}} \right) \quad (6)$$

The final alignment loss is as shown in Eq. 7. The weight coefficients  $\beta_1, \beta_2, \beta_3$  and  $\beta_4$  are set as  $\beta_1 = 0.2, \beta_2 = 0.3, \beta_3 = 0.2, \beta_4 = 0.3$ .

$$\mathcal{L}_{align} = \beta_1 \mathcal{L}_{img} + \beta_2 \mathcal{L}_{glo} + \beta_3 \mathcal{L}_{loc} + \beta_4 \mathcal{L}_{soft}. \quad (7)$$

Following feature alignment, the image backbone undergoes supervised refinement using ground-truth labels and Cross-Entropy loss [14]. This stage sharpens visual representations by bridging the gap between general cross-modal alignment and task-specific diagnostic requirements.

### 2.3 Feature Integration via Large Language Model

To leverage Large Language Model reasoning, we bridge the gap between encoders and the LLM backbone via a multi-modal projection strategy. Global tokens are projected using MLP layers, while local sequence tokens are aligned through 1D/2D convolution blocks that perform spatial/temporal downsampling to reduce overhead. These features are concatenated into an input sequence demarcated by learnable special tokens (e.g.,  $\langle \text{img\_start} | \rangle$ ), which are initialized with semantic embeddings to accelerate convergence. To maintain efficiency and prevent overfitting, we utilize LoRA [6], updating only the projectors and  $\sim 1\%$  of total parameters. We further employ a vocabulary-restricted strategy to eliminate hallucinations: instead of free-form generation, we extract logits  $z_k$  exclusively from a token subset  $\mathcal{C}$  corresponding to pre-defined clinical classes. Probabilities are computed via Softmax over this constrained set:  $P(y = k|x) = \frac{\exp(z_k)}{\sum_{j \in \mathcal{C}} \exp(z_j)}$ . The model is optimized by Cross Entropy loss [14].

### 3 Experiment and Result

**Dataset Details** We evaluated PRIMA on two benchmarks. PAD-UFES-20 [16] contains 2,298 images of 1,891 lesions from 1,373 patients across six categories: Basal Cell Carcinoma (BCC), Squamous Cell Carcinoma (SCC), Actinic Keratosis (ACK), Seborrheic Keratosis (SEK), Melanoma (MEL), and Nevus (NEV). AQUA, a private dataset collected at anonymized medical centers under an approved IRB protocol ([Anonymized for Review]), comprises 19,567 slit-lamp photography (SLP) images from 1,827 subjects. It focuses on bacterial and fungal keratitis using three modalities: diffuse white light, diffuse blue light, and sclerotic scatter illumination. We adopted a lesion-level split for PAD-UFES-20 and a patient-level split for AQUA. We employed five-fold cross-validation and evaluated performance using F1-score, accuracy, and balanced accuracy (BAcc).

**Implementation Details** PRIMA is trained on two NVIDIA RTX 4090 GPUs (24GB) using AdamW and a cosine scheduler with 10% warm-up. Hyperparameters across the three stages are: Stage 1 (LR 5e-5, WD 1e-3, 2500 epochs), Stage 2 (LR 3e-5, WD 1e-3, 150 epochs), and Stage 3 (LR 1e-5, WD 3e-2, 80 epochs). LoRA ranks are set to 8, 32, and 16 for our text encoder, our image encoder, and the LLM, respectively. Our code will be public upon acceptance.

#### 3.1 Main Results

We evaluated PRIMA against several prominent baselines across two datasets. To establish a rigorous reference, we first fine-tuned DINOv3 [20] via LoRA as a pure-image baseline. We then combined these visual features with vanilla Clinical ModernBERT [7] embeddings using an MLP to assess the impact of simple multi-modal fusion. Furthermore, we compared PRIMA against specialized diagnostic networks: DeepIK [9], which employs a CNN-based architecture specifically for keratitis diagnosis; MedKLIP [23], which proposes a Transformer-based fusion module to integrate multi-modal visual and textual information; and KnoBo [25], which first projects image features into a symbolic concept space to facilitate clinical decision-making. Finally, we included MedBLIP [2] and MLRG [12], which leverage LLMs for feature aggregation through diverse training strategies.

Results in Tables 1-2 show that while DINOv3 provides a high performance floor, PRIMA consistently yields a  $> 5\%$  accuracy boost via multi-granular alignment, confirming that expert prior injection is vital where generic visual strength is insufficient. PRIMA achieves state-of-the-art results on PAD-UFES-20 (F1: 73.75%, Acc: 78.27%) and AQUA (F1: 85.22%, Acc: 86.04%), surpassing all competitors. The performance drop of specialized methods (MedKLIP, KnoBo) on PAD-UFES-20 underscores their limited transferability compared to our holistic strategy. While LLM-based baselines (MedBLIP, MLRG) perform strongly, our optimized training and knowledge injection consistently yield superior feature integration. Although PAD-UFES-20 metadata could theoretically appear in some foundation models’ pre-training corpora, we mitigate this by using LLMs solely for offline knowledge extraction without patient data interaction.

Crucially, PRIMA’s significant gains on the private AQUA dataset—entirely inaccessible to foundation models—validate that our performance stems from the proposed alignment strategy rather than data memorization.

Table 1: Quantitative results of PAD-UFES-20 dataset (%). SD in parentheses.

Methods	BCC	SCC	MEL	ACK	SEK	NEV	Avg F1-score	Acc	BAcc
DINOv3 (ArXiv-25) [20] LoRA + Metadata via MLP	72.23 (1.76)	32.55 (5.80)	70.41 (13.35)	79.38 (1.36)	76.72 (3.35)	76.90 (4.58)	68.03 (2.48)	71.07 (0.83)	69.66 (3.53)
MedKLiP (ICCV-23) [23]	54.10 (6.87)	16.08 (3.59)	21.85 (18.08)	61.99 (3.53)	47.81 (3.14)	55.24 (7.17)	42.84 (4.77)	51.29 (3.59)	43.81 (5.10)
KnoBo (NIPS-24) [25]	63.33 (3.40)	23.04 (6.47)	33.32 (22.43)	70.80 (1.99)	32.25 (9.48)	63.75 (8.56)	47.75 (4.91)	58.80 (2.63)	50.89 (5.77)
MedBLiP (ACCV-24) [2]	77.24 (4.29)	38.37 (5.00)	77.60 (13.21)	81.18 (2.40)	76.08 (4.31)	81.61 (5.53)	72.01 (2.36)	75.41 (2.58)	72.32 (3.01)
MLRG (CVPR-25) [12]	73.70 (8.11)	23.45 (8.56)	62.36 (13.17)	81.39 (2.12)	59.34 (1.79)	69.00 (4.56)	61.54 (4.11)	70.65 (4.55)	60.28 (4.79)
<b>PRIMA (Ours)</b>	<b>80.21 (1.19)</b>	<b>37.33 (7.86)</b>	<b>85.84 (8.35)</b>	<b>85.73 (2.23)</b>	<b>73.10 (5.77)</b>	<b>80.26 (6.07)</b>	<b>73.75 (3.40)</b>	<b>78.27 (1.78)</b>	<b>72.76 (2.86)</b>

Table 2: Quantitative results of AQUA dataset (%). SD in parentheses.

Methods	Fungal	Bacterial	Avg F1-score	Acc	BAcc
DINOv3 (ArXiv-25) [20] LoRA + Metadata via MLP	82.54 (1.44)	71.42 (2.74)	76.98 (1.78)	78.37 (1.60)	78.25 (1.42)
DeepIK (NPJ Dig. Med-24) [9]	80.84 (2.58)	76.54 (3.56)	78.69 (3.00)	78.93 (2.94)	81.11 (2.38)
KnoBo (NIPS-24) [25]	83.54 (4.62)	72.42 (7.71)	77.98 (6.09)	79.42 (5.72)	77.76 (5.75)
MedBLiP (ACCV-24) [2]	80.96 (6.41)	75.55 (4.67)	78.26 (5.13)	78.82 (5.37)	79.86 (4.34)
MLRG (CVPR-25) [12]	83.35 (2.36)	74.28 (4.32)	78.81 (2.73)	79.91 (2.44)	79.15 (2.81)
<b>PRIMA (Ours)</b>	<b>88.66 (1.22)</b>	<b>81.78 (3.21)</b>	<b>85.22 (2.17)</b>	<b>86.04 (1.82)</b>	<b>85.40 (2.27)</b>

Table 3: Ablation study of PAD-UFES-20 dataset (%).

Knowledge Pretraining	$\mathcal{L}_{img}$	$\mathcal{L}_{glo}$	$\mathcal{L}_{loc}$	$\mathcal{L}_{soft}$	$\mathcal{L}_{loc\_dir}$	$\mathcal{L}_{sup\_con}$	Avg F1-score	Acc	BAcc
✓	✓	✓	✓	✓	✓	✓	67.94 (3.88)	75.25 (3.85)	66.20 (3.50)
✓	✓	✓	✓	✓	✓	✓	68.41 (4.19)	74.78 (3.82)	67.70 (3.54)
✓	✓	✓	✓	✓	✓	✓	68.49 (3.34)	75.99 (2.97)	67.79 (3.87)
✓	✓	✓	✓	✓	✓	✓	70.36 (2.48)	76.63 (1.90)	69.69 (3.05)
✓	✓	✓	✓	✓	✓	✓	72.42 (2.35)	76.42 (3.19)	72.09 (3.45)
✓	✓	✓	✓	✓	✓	✓	72.88 (3.23)	77.84 (3.54)	71.80 (2.19)
✓	✓	✓	✓	✓	✓	✓	70.02 (3.80)	77.47 (3.35)	68.53 (4.25)
✓	✓	✓	✓	✓	✓	✓	71.42 (2.96)	76.15 (3.03)	72.05 (2.43)
✓	✓	✓	✓	✓	✓	✓	<b>73.75 (3.40)</b>	<b>78.27 (1.78)</b>	<b>72.76 (2.86)</b>

### 3.2 Ablation Study

Ablation results (Table 3) justify each component’s role. While LLMs possess inherent representational power, they struggle under limited medical supervision, evidenced by the performance drop when trained solely on class labels. Integrating Image Consistency Loss ( $\mathcal{L}_{img}$ ) enhances visual robustness, though cross-modal alignment remains unaddressed. Global Semantic Loss ( $\mathcal{L}_{glo}$ ) provides essential high-level synchronization, whereas Local Semantic Loss ( $\mathcal{L}_{loc}$ ) establishes fine-grained correspondences between local image regions and textual tokens. Furthermore, Soft Semantic Loss ( $\mathcal{L}_{soft}$ ) leverages clinical metadata to incorporate complex relationships during feature aggregation. Finally, injecting domain-specific priors significantly sharpens the model’s grasp of clinical nuances, with their synergy achieving PRIMA’s optimal performance. To further validate our designs, we evaluated simplified variants: removing the attention mechanism from  $\mathcal{L}_{loc}$  (denoted  $\mathcal{L}_{loc\_dir}$ ) and restricting  $\mathcal{L}_{soft}$  to basic class labels (denoted  $\mathcal{L}_{sup\_con}$ ). The resulting performance degradation underscores the necessity of our multi-granular and metadata-aware formulations.

## 4 Conclusion

We introduce PRIMA, which integrates Clinical ModernBERT, pre-trained on an expert medical corpus, with DINOv3 to align diagnostic priors with robust visual representations. Four multi-granular losses synchronize these components to capture precise clinical correspondences. With Qwen-3 orchestrating the final multi-modal fusion, PRIMA achieves state-of-the-art accuracy and high efficiency without requiring massive compute. We acknowledge two limitations: the need for backbone-controlled experiments to isolate alignment gains from encoder strength, and potential generational biases among LLMs of similar scales. These aspects will be addressed in a subsequent journal extension.

## References

1. Amugongo, L.M., Mascheroni, P., Brooks, S., Doering, S., Seidel, J.: Retrieval augmented generation for large language models in healthcare: A systematic review. *PLOS Digital Health* **4**(6), e0000877 (2025)
2. Chen, Q., Hong, Y.: Medblip: Bootstrapping language-image pre-training from 3d medical images and texts. In: *Proceedings of the Asian conference on computer vision*. pp. 2404–2420 (2024)
3. Comanici, G., Bieber, E., Schaeckermann, M., Pasupat, I., Sachdeva, N., Dhillon, I., Blistein, M., Ram, O., Zhang, D., Rosen, E., et al.: Gemini 2.5: Pushing the frontier with advanced reasoning, multimodality, long context, and next generation agentic capabilities. *arXiv preprint arXiv:2507.06261* (2025)
4. Devlin, J., Chang, M.W., Lee, K., Toutanova, K.: Bert: Pre-training of deep bidirectional transformers for language understanding. In: *Proceedings of the 2019 conference of the North American chapter of the association for computational linguistics: human language technologies, volume 1 (long and short papers)*. pp. 4171–4186 (2019)
5. Du, J., Guo, J., Zhang, W., Yang, S., Liu, H., Li, H., Wang, N.: Ret-clip: A retinal image foundation model pre-trained with clinical diagnostic reports. In: *International conference on medical image computing and computer-assisted intervention*. pp. 709–719. Springer (2024)
6. Hu, E.J., Shen, Y., Wallis, P., Allen-Zhu, Z., Li, Y., Wang, S., Wang, L., Chen, W., et al.: Lora: Low-rank adaptation of large language models. *Iclr* **1**(2), 3 (2022)
7. Lee, S.A., Wu, A., Chiang, J.N.: Clinical modernbert: An efficient and long context encoder for biomedical text. *arXiv preprint arXiv:2504.03964* (2025)
8. Li, C., Wong, C., Zhang, S., Usuyama, N., Liu, H., Yang, J., Naumann, T., Poon, H., Gao, J.: Llava-med: Training a large language-and-vision assistant for biomedicine in one day. *Advances in Neural Information Processing Systems* **36**, 28541–28564 (2023)
9. Li, Z., Xie, H., Wang, Z., Li, D., Chen, K., Zong, X., Qiang, W., Wen, F., Deng, Z., Chen, L., et al.: Deep learning for multi-type infectious keratitis diagnosis: a nationwide, cross-sectional, multicenter study. *NPJ Digital Medicine* **7**(1), 181 (2024)
10. Li, Z., Wang, Y., Farsiu, S., Kinahan, P.: Boosting medical visual understanding from multi-granular language learning. *arXiv preprint arXiv:2511.15943* (2025)
11. Lindberg, D.: Internet access to the national library of medicine. *Effective clinical practice* **3**(5) (2000)

12. Liu, K., Ma, Z., Kang, X., Li, Y., Xie, K., Jiao, Z., Miao, Q.: Enhanced contrastive learning with multi-view longitudinal data for chest x-ray report generation. In: Proceedings of the Computer Vision and Pattern Recognition Conference. pp. 10348–10359 (2025)
13. Lu, S., Liu, J., Wang, X., Zhou, Y.: Collaborative multi-metadata fusion to improve the classification of lumbar disc herniation. *IEEE Transactions on Medical Imaging* **42**(12), 3590–3601 (2023)
14. Mao, A., Mohri, M., Zhong, Y.: Cross-entropy loss functions: Theoretical analysis and applications. In: International conference on Machine learning. pp. 23803–23828. pmlr (2023)
15. OpenAI: Openai 5.1 system card. [https://cdn.openai.com/pdf/4173ec8d-1229-47db-96de-06d87147e07e/5\\_1\\_system\\_card.pdf](https://cdn.openai.com/pdf/4173ec8d-1229-47db-96de-06d87147e07e/5_1_system_card.pdf) (2026), accessed: 2026-02-23
16. Pacheco, A.G.C., Lima, G.R., da Silva Salomão, A., Krohling, B., Biral, I.P., de Angelo, G.G., Jr, F.C.A., Esgario, J.G.M., Simora, A.C., Castro, P.B.C., Rodrigues, F.B., Frasson, P.H.L., Krohling, R.A., Knidel, H., Santos, M.C.S., do Espírito Santo, R.B., Macedo, T.L., Canuto, T.R.P., de Barros, L.F.: Pad-ufes-20: A skin lesion dataset composed of patient data and clinical images collected from smartphones. *Data in Brief* **32** (2020)
17. Pacheco, A.G., Krohling, R.A.: An attention-based mechanism to combine images and metadata in deep learning models applied to skin cancer classification. *IEEE journal of biomedical and health informatics* **25**(9), 3554–3563 (2021)
18. Radford, A., Kim, J.W., Hallacy, C., Ramesh, A., Goh, G., Agarwal, S., Sastry, G., Askell, A., Mishkin, P., Clark, J., et al.: Learning transferable visual models from natural language supervision. In: International conference on machine learning. pp. 8748–8763. PmLR (2021)
19. Silva-Rodriguez, J., Chakor, H., Kobbi, R., Dolz, J., Ayed, I.B.: A foundation language-image model of the retina (flair): Encoding expert knowledge in text supervision. *Medical Image Analysis* **99**, 103357 (2025)
20. Siméoni, O., Vo, H.V., Seitzer, M., Baldassarre, F., Oquab, M., Jose, C., Khalidov, V., Szafraniec, M., Yi, S., Ramamonjisoa, M., et al.: Dinov3. arXiv preprint arXiv:2508.10104 (2025)
21. Wang, H., Guo, S., Ye, J., Deng, Z., Cheng, J., Li, T., Chen, J., Su, Y., Huang, Z., Shen, Y., et al.: Sam-med3d: a vision foundation model for general-purpose segmentation on volumetric medical images. *IEEE Transactions on Neural Networks and Learning Systems* (2025)
22. Wang, Z., Wu, Z., Agarwal, D., Sun, J.: Medclip: Contrastive learning from unpaired medical images and text. In: Proceedings of the 2022 Conference on Empirical Methods in Natural Language Processing. pp. 3876–3887 (2022)
23. Wu, C., Zhang, X., Zhang, Y., Wang, Y., Xie, W.: Medklip: Medical knowledge enhanced language-image pre-training for x-ray diagnosis. In: Proceedings of the IEEE/CVF international conference on computer vision. pp. 21372–21383 (2023)
24. Yang, A., Li, A., Yang, B., Zhang, B., Hui, B., Zheng, B., Yu, B., Gao, C., Huang, C., Lv, C., Zheng, C., Liu, D., Zhou, F., Huang, F., Hu, F., Ge, H., Wei, H., Lin, H., Tang, J., Yang, J., Tu, J., Zhang, J., Yang, J., Yang, J., Zhou, J., Zhou, J., Lin, J., Dang, K., Bao, K., Yang, K., Yu, L., Deng, L., Li, M., Xue, M., Li, M., Zhang, P., Wang, P., Zhu, Q., Men, R., Gao, R., Liu, S., Luo, S., Li, T., Tang, T., Yin, W., Ren, X., Wang, X., Zhang, X., Ren, X., Fan, Y., Su, Y., Zhang, Y., Zhang, Y., Wan, Y., Liu, Y., Wang, Z., Cui, Z., Zhang, Z., Zhou, Z., Qiu, Z.: Qwen3 technical report. arXiv preprint arXiv:2505.09388 (2025)

25. Yang, Y., Gandhi, M., Wang, Y., Wu, Y., Yao, M., Callison-Burch, C., Gee, J., Yatskar, M.: A textbook remedy for domain shifts: Knowledge priors for medical image analysis. *Advances in neural information processing systems* **37**, 90683–90713 (2024)